JGR Space Physics

RESEARCH ARTICLE
10.1029/2019JA027371

Key Points:
- A temporally variable magnetotail current sheet is observed at Saturn during the F-ring apoapsis passes
- The variability can be explained by two rotating magnetic perturbation sources and variable solar wind forcing
- Results are consistent with a regime where the northern system is dominant with an amplitude ratio of ~1.3

Correspondence to:
O. Agiwal,
o.agiwal17@imperial.ac.uk

Citation:
Agiwal, O., Hunt, G. J., Dougherty, M. K., Cowley, S. W. H., & Provan, G. (2020). Modeling the temporal variability in Saturn's magnetotail current sheet from the Cassini F-ring orbits. *Space Physics Space Physics*, *125*, e2019JA027371. https://doi.org/10.1029/2019JA027371

Received 3 SEP 2019
Accepted 14 NOV 2019
Accepted article online 11 DEC 2019

Modeling the Temporal Variability in Saturn's Magnetotail Current Sheet From the Cassini F-ring Orbits

O. Agiwal[1], G. J. Hunt[1], M. K. Dougherty[1], S. W. H. Cowley[2], and G. Provan[2]

[1]Blackett Laboratory, Imperial College London, London, UK, [2]Department of Physics and Astronomy, University of Leicester, Leicester, UK

Abstract The Cassini spacecraft completed 20 highly repeatable orbits during northern summer at Saturn, known as the F-ring orbits, of which 18 are considered in this study. The spacecraft traversed Saturn's magnetotail current sheet during each apoapsis pass between 16 and 22 Saturn radii over 2-day intervals and revealed a highly variable radial magnetic field from orbit to orbit. The solar wind and planetary period oscillations (PPOs) are significant sources of temporal variability in the Saturnian magnetosphere. PPOs refer to dual magnetic perturbation systems, one in each hemisphere, which have been observed to modulate the position and thickness of the magnetotail current sheet with a ~10.7-hr periodicity. Thus, we employ a model which considers dual-modulation effects of the northern and southern PPO systems, together with a model of variable solar wind forcing on the magnetotail current sheet, to investigate their combined temporal effects on the radial magnetic field in the magnetotail. For all 18 F-ring orbits considered, the modeled radial fields show excellent overall agreement with the temporal variability in the large-scale structure of the observed radial fields (root mean square error <1.5 nT for 80% of the orbits). The amplitudes of the northern PPO modulations are well constrained between 0.3 and 0.5 Saturn radii, and they exceed the southern modulations by a factor of 1.3. The solar wind forcing is observed to be highly variable from orbit to orbit.

1. Introduction

The Cassini spacecraft completed 20 orbits (Revs 251–270), known as the “F-ring” orbits, between 30 Nov 2016 and 22 Apr 2017, an interval corresponding to northern summer at Saturn. The spacecraft trajectory was highly repeatable from orbit to orbit, with a minor drift (~30 min in total) in local time. During approach to orbit apoapsis at $\sim 21R_S$, the spacecraft traversed the equatorial current sheet in the nightside magnetosphere, which separates the northern and southern magnetotail lobes, as it transitioned from the southern hemisphere to the northern hemisphere. Encounters with the magnetic equator, which corresponds to the center of the magnetotail current sheet, are identified by a reversal in the sense of the radial component of the magnetic field B_r, which is positive northward of the magnetic equator and negative southward. The magnetic field observations from the magnetometer on board the Cassini spacecraft are highly variable from orbit to orbit near apoapsis. Despite the repeatable trajectory, the spacecraft encounters the magnetic equator at variable positions in each Rev, and in some cases, multiple reversals in the field were observed on a given orbit.

The results from the Cassini Grand Finale presented by Dougherty et al. (2018) showed that the tilt between the magnetic and rotational axes at Saturn is $< 0.0095°$, with a slight northward offset of the magnetic equator from the rotational equator by $0.047R_S$ ($1R_S = 60,268$ km). However, Arridge et al. (2008) presented evidence of a much larger northward displacement of the magnetic equator in the nightside magnetic field data taken during southern hemisphere summer at Saturn. Arridge et al. (2008) suggested that this displacement is due to the solar wind forcing the configuration of the magnetic field, and thus, the direction of the displacement would change with Saturnian season. They presented a model (henceforth the Arridge model) which evaluates the position of the displaced magnetic equator: The displacement effect in their model gradually increases with radial distance from the planet, and the point at which displacement becomes significant ($\rho = \rho_H$) is known as the “hinging distance.” A smaller value of ρ_H implies that the offset between the rotational and magnetic equators becomes significant closer to the planet and increases

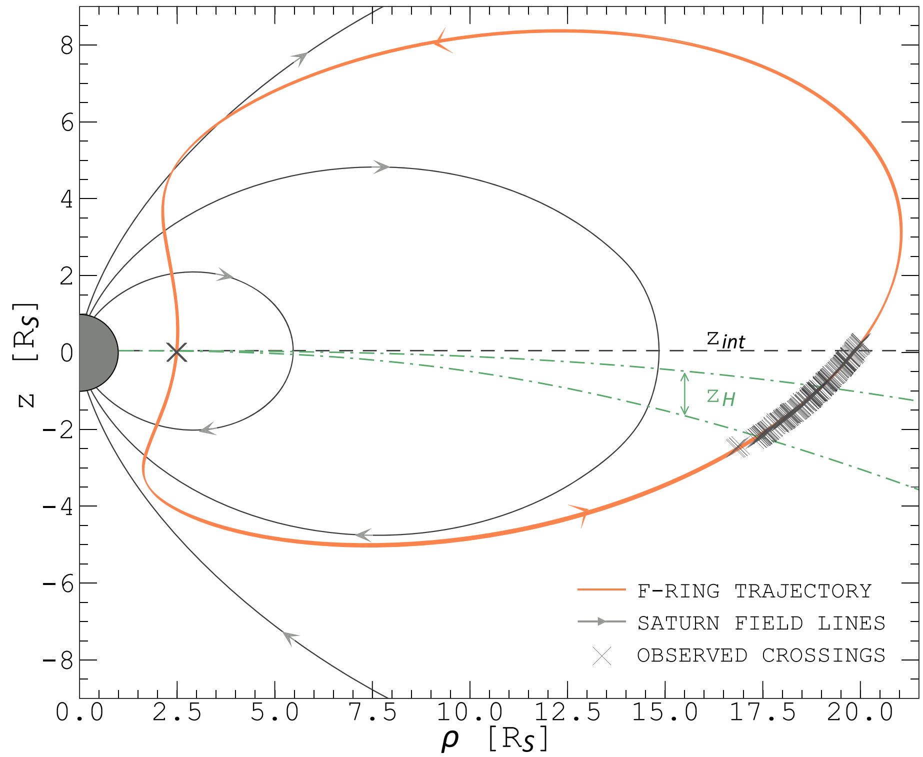

Figure 1. The trajectory of the Cassini Revs 251–269 is shown superposed by the solid orange line in (ρ, z) coordinates where z is aligned with the Saturn spin/dipole axis and ρ is the perpendicular distance from z. Saturn is centered at the origin. The magnetospheric field (degree-3 internal field model + magnetodisk (Connerney et al., 1981)) is illustrated by solid gray lines with arrows. The dashed black line is the magnetic equator evaluated by the internal field model, z_{int}. The dot-dashed green lines are the magnetic equator as evaluated by the Arridge model for Northern Saturnian Summer at two hinging distances, $\rho_H = 16R_S$ (lower line) and $\rho_H = 32R_S$ (upper line). The black crosses on the spacecraft trajectory indicate the locations of every encounter with the magnetic equator ($B_r = 0$) observed in the magnetic field data.

in the tailward direction. A later study by Arridge et al. (2011) showed that ρ_H was highly variable over month-long timescales in the nightside magnetosphere during southern summer, ranging from 16 to $32R_S$, which is consistent with our observations of a temporally variable magnetic equator.

The spacecraft trajectory for Revs 251–269 is shown by a solid orange line in Figure 1, in a cylindrical (ρ, z) coordinate system, where z is aligned with the planetary spin/dipole axis and ρ is the perpendicular distance from z. Rev 270 is excluded from this discussion as the spacecraft trajectory changed at orbit apoapsis for the Cassini Grand Finale orbits. The superposition of the trajectories illustrates the extent of the repeatability in a (ρ, z) coordinate system. The location of every B_r reversal observed in the magnetic field data is indicated by black crosses on the trajectory. The position of the hinged magnetic equator z_H evaluated by the Arridge model for northern summer is shown by dot-dashed green lines in Figure 1, for $\rho_H = 16R_S$ (lower line) and $\rho_H = 32R_S$ (higher line).

At orbit periapsis, a single B_r reversal is observed per Rev, and the location of the reversal is repeatable from orbit to orbit, thus indicating that the magnetic equator is temporally static. However, the B_r reversals near orbit apoapsis are observed over a large range of (ρ, z) positions, only half of which occur in the region confined between the two dot-dashed green lines. The reversals observed at $z > z_{int}$, the expected position of the magnetic equator due to the internally generated planetary field, are inconsistent with the southward displacement of the magnetic equator predicted by the Arridge model for northern summer and are therefore indicative of additional perturbation sources modulating the magnetotail. Additionally, the multiple B_r reversals observed on individual orbits indicate that the position of the magnetic equator is variable over hour-long timescales, which is much too rapid to be solar wind driven.

Large-scale vertical motions of the magnetotail current sheet have previously been reported at Saturn (Jackman et al., 2009; Khurana et al., 2009; Szego et al., 2013; Thomsen et al., 2017) and linked to the perturbations known as planetary period oscillations (PPOs) (Cowley et al., 2017; Provan et al., 2012; Thomsen et al., 2017). PPOs refer to ~10.7-hr modulation features which have been observed in the data set of all magnetospheric parameters at Saturn (see review by Carbary and Mitchell (2013) and references therein). Both magnetic field and Saturn kilometric radiation observations have indicated the presence of two separate perturbation periods, in the northern and southern hemispheres, respectively, and were used to determine the dual periodicities for the entire Cassini Mission (Andrews et al., 2008, 2012; Cowley & Provan, 2015, 2016; Gurnett, 2011; Gurnett et al., 2009; Kurth et al., 2007, 2008; Lamy, 2011, 2017; Provan et al., 2013, 2014, 2016, 2019).

The two PPO systems are driven by polar ionospheric flows in the northern and southern hemispheres, which set up field-aligned current systems that rotate independently around Saturn's spin/dipole axis with rotation periods close to the expected planetary rotation period of ~10.7 hr (Hunt et al., 2014, 2015, 2016; Jia & Kivelson, 2012; Southwood & Kivelson, 2007; Southwood & Cowley, 2014). Each system produces a quasi-uniform perturbation field in the equatorial region that closes over the corresponding pole as a quasi-dipolar field. Provan et al. (2012) presented magnetotail data from 2006, showing that observations from the equatorial region were dual modulated by the two PPO systems. The position of each system relative to local noon is described by a phase angle $\Phi_{N,S}$, such that the relative phase $\Delta\Phi$ between the two rotating systems is given by

$$\Delta\Phi = \Phi_N - \Phi_S, \tag{1}$$

a quantity that is referred to as the "beat phase" between the two systems. Provan et al. (2012) showed that strong north-south displacements of the tail current sheet were observed when the systems were in phase ($\Delta\Phi = 0°$), while strong thickness modulations were observed when they were in antiphase($\Delta\Phi = 180°$).

Studies carried out on tail data from a similar interval have also shown modulations in current sheet thickness (Cowley & Provan, 2017; Morooka et al., 2009; Thomsen et al., 2017). Thomsen et al. (2017) observed periodic reversals in B_r every ~10.7 hr in magnetotail data from 2010, despite the spacecraft traveling at a nearly constant z position. In certain cases the observations presented "sawtooth" asymmetries, where the north-south current sheet crossings occurred faster than the south-north, and vice versa. They attributed these asymmetries to a current sheet that underwent periodic thickness modulations when $\Delta\Phi \sim 90°/270°$. A simple mathematical model proposed by Cowley et al. (2017) (C17) considers the effects of the two PPO systems on a simple Harris current sheet and thus the radial magnetic field in the nightside equatorial region. The model has successfully described the current sheet crossings observed in magnetic field data (Cowley & Provan, 2017; Cowley et al., 2017; Thomsen et al., 2017) from intervals where the spacecraft conducted long-term equatorial orbits.

In this study, we will combine the C17 method with the Arridge hinge (with a variable hinging distance in northern summer conditions) to model the PPO modulated radial magnetic field along the spacecraft trajectory for each Rev of the F-ring orbits. By using repeatable and highly inclined orbits as a novel approach to study the variability in the Saturnian current sheet, the short-term temporal effect of the PPO systems and the solar wind hinging can be explored in a large spatial region of the magnetosphere, over an interval of ~5 months. Comparison between the model output and the data will determine if the orbit-to-orbit variability observed in the magnetic field data is consistent with PPO modulations and variable solar wind forcing of the magnetotail current sheet.

1.1. The Data

The B_r observations from the outbound leg of the F-ring orbits (Revs 251–269, excluding Rev 270), where the spacecraft traversed the magnetotail current sheet, are presented in Figure 2. Each panel in Figure 2 shows the measurements taken approximately in the cylindrical radial range between 16 and 20–21R_S, and consecutive orbits occur approximately 1 week apart. The data are shown at 1-min resolution, with each pass showing a clear transition from south of the current sheet center ($B_r < 0$ nT) to north of the center ($B_r > 0$ nT), with superposed modulations near the ~10.7-hr PPO period. The spacecraft traversed this distance in 1.5–2 days on average, where the exact interval shown in each panel is variable, as it is selected to include some data from the northern and southern magnetic lobes while keeping the focus on the B_r reversals.

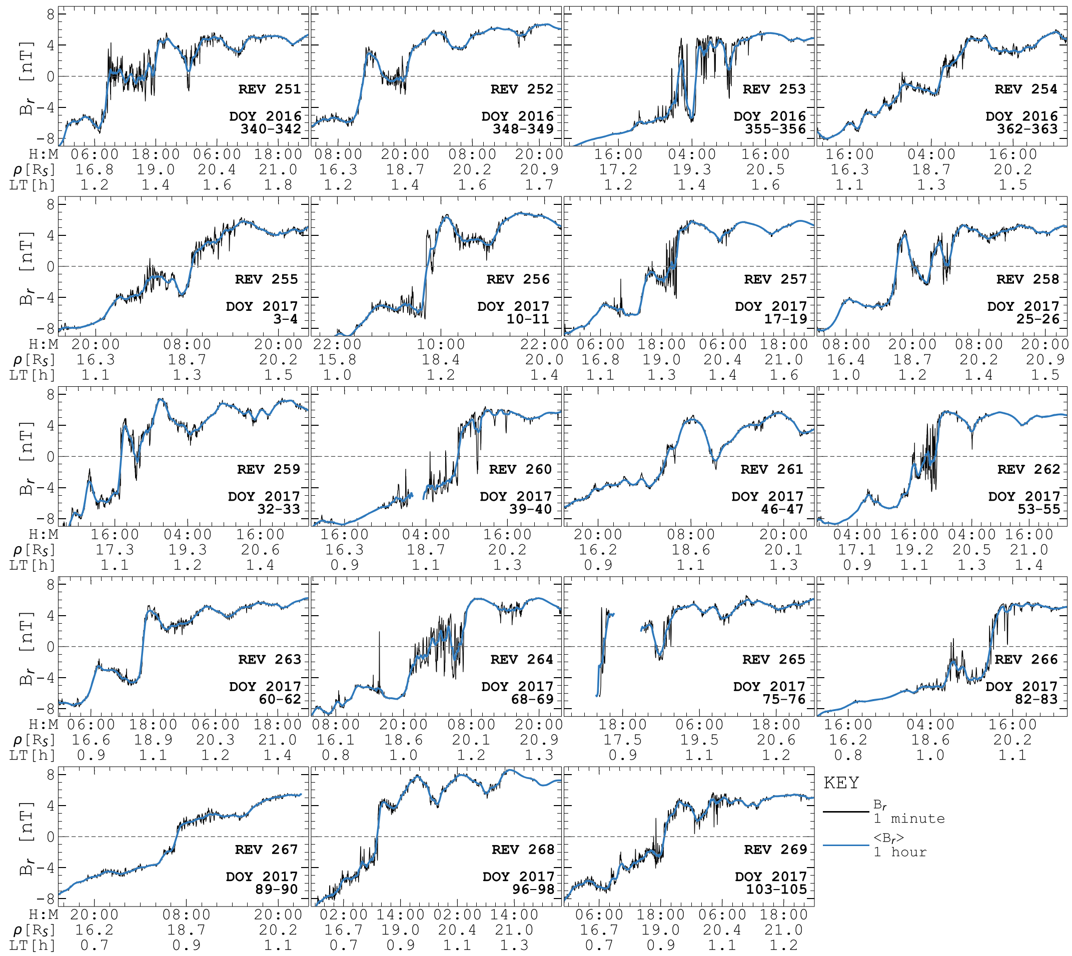

Figure 2. The radial component of the magnetic field B_r at 1-min resolution is shown by the solid black line for the outbound legs of Revs 251–269. The observations presented were made while the spacecraft was in the post-midnight local time sector and in the region between $\rho \simeq 16$ and $21R_S$ in each panel. The magnetic field data are highly variable from orbit to orbit despite the near-consistent spacecraft trajectory. A solid blue line shows the 1-hr running average of the magnetic field data, $\langle B_r \rangle$. The data from Rev 265 are omitted from this study due to the large data gaps in our region of interest.

It is evident that there is significant orbit-to-orbit variability in the B_r profiles presented in Figure 2. For example, in Revs 251–253, there are several fluctuations in B_r on the order of 10–20 min, which is much shorter than the expected PPO dynamic timescales (<2 hr). The fluctuations have variable amplitudes, where the smaller fluctuations are ~1–2 nT in magnitude (e.g., Rev 254) but the larger fluctuations are ~4–6 nT (e.g., Rev 251). These fluctuations are seen in all Revs to some extent, but in Revs 251–253, 257, 258, 262, and 264, it coincides with successive reversals in B_r, implying rapid north-south movement of the magnetotail current sheet, on a timescale much shorter than the PPO modulation period.

In addition, the B_r reversals are observed over a range of ρ positions: The first encounter with the current sheet occurs further downtail ($\rho > 18R_S$) on Revs 253, 257, 262, 264, 266, and 269, as compared to the other Revs, which could be related to other perturbation sources such as solar wind hinging effects. Revs 254, 255, 260, and 266 are similar to each other, as B_r tends toward zero but increases in magnitude once again before the reversal actually occurs, which is consistent with our understanding of a periodically modulated current sheet which is moving away from the spacecraft. Revs 256, 263, and 267 are the only orbits where a single B_r reversal is observed. It is thus evident that a range of variable behaviors is present in this data set.

The primary objective of this work, however, is to understand whether PPO modulations combined with solar wind hinging can explain the variability of the large-scale structure of the B_r profiles and the variable positions of the B_r reversals. To focus on this, we take a 1-hr running average of the magnetic field data,

$\langle B_r \rangle$, which are also shown for every Rev in Figure 2 as solid blue lines, which will be used for comparison between the large-scale structures of B_r with the output radial field of the C17 model in section 3, since the C17 model is not expected to capture this short timescale detail. The source of the small-timescale structure in B_r is still of interest, and we aim to use the C17 and Arridge models to investigate correlations between the small-timescale structure and a temporally modulated current sheet.

2. Method

2.1. The Theoretical Model

The C17 method models the dual-modulation effect of northern and southern PPO phases on a simple Harris current sheet. The local phase of each PPO perturbation system $\Psi_{N,S}$ for an observer at radial position r outside the core region of the PPO field ($> 12R_S$) is determined using

$$\Psi_{N,S}(r, \varphi, t) = \Phi_{N,S}(t) - \varphi_{sc}(t) - G[r(t) - 12R_S], \tag{2}$$

where $\Phi_{N,S}(t)$ is the phase angle from the noon meridian to where the near-equatorial quasi-uniform PPO fields point radially outward from Saturn and $\varphi_{sc}(t)$ is the azimuthal position of the observer relative to the noon meridian. The phase angles $\Phi_{N,S}(t)$ for the F-ring interval have been evaluated by Provan et al. (2018). The angles increase in the direction of planetary rotation, that is, noon to dusk, with fixed periods of 10.792 hr for the northern system and 10.679 hr for the southern system. The final term in equation (2) accounts for a delay in phase which is observed outside the core region of the PPO field, where $G = 3^\circ R_S^{-1}$ is the radial phase gradient (Arridge et al., 2011; Provan et al., 2012). In this study, equation (2) is evaluated along the spacecraft trajectory.

C17 and Cowley and Provan (2017) show that the radial field, $B_r(t)$, measured by an observer/spacecraft at position $z_{sc}(t)$ traveling through two superimposed Harris current sheets with a displaced center at $z^*(t)$ and modulated half-thickness of $D^*(t)$ can be determined using

$$\frac{B_r(t)}{B_{lobe}} = a \tanh\left[\frac{z_{sc}(t) - z^*(t)}{D^*(t)}\right] + \quad b \tanh\left[\frac{z_{sc}(t) - z^*(t)}{cD^*(t)}\right], \tag{3}$$

where a, b, and c are constants indicating the relative strengths and thickness (respectively) of two current sheets. These constants are approximated to be $a = 0.7$, $b = (1 - a)$, and $c = 5$ by C17. The first term represents a narrow sheet, embedded within a weaker and more diffuse secondary layer represented by the second term to allow for a more realistic, smaller-gradient boundary between the current sheet and the lobes as observed by (Cowley & Provan, 2017). The z position of the spacecraft relative to the rotational equator is z_{sc}, and the PPO modulated position of the magnetic equator and half-thickness of the current sheet are z^* and D^*, respectively. B_{lobe} is the magnetic field strength of the magnetotail lobes, which varies with radial distance r, from the planet. An empirical model presented by Jackman and Arridge (2011) estimates the relationship between B_{lobe} and r to be

$$B_{lobe} = (125 \pm 22) \times (r^{-1.20\pm0.03}), \tag{4}$$

where B_{lobe} is in nT, r is in R_S, and the model is only valid at $r \geq 15R_S$ in the nightside magnetosphere. Due to the asymmetric north-south geometry of the spacecraft trajectory (as shown in Figure 1) and the spatial and temporal magnetic perturbation sources considered in this study, the spacecraft encounters the northern and southern magnetotail lobes at different radial positions and for variable time intervals in each F-ring orbit.

Analysis of the total magnetic field strength averaged over 11 hr (approximately one PPO cycle) shows that the spacecraft is in a stable magnetic field region, which is indicative of the magnetotail lobes, at $\sim 16R_S$ in the southern hemisphere and $\sim 20R_S$ in the northern hemisphere for every F-ring orbit. However, the magnetic field strength measured at these positions is variable from orbit to orbit. We find that the data are well matched by one of four iterations of equation (4), with the following error limits on the first and second brackets, respectively: $[-22, -0.03]$, $[-22, 0]$, $[0, 0]$, and $[22, 0]$. This corresponds to B_{lobe} values at $(16, 21)R_S$ of (7.6, 5.4) nT, (8.2, 5.9) nT, (9.0, 6.5) nT, and (9.8, 7.1) nT, respectively.

In our method, we utilize the B_{lobe} profile that most closely matches the average lobe field strength observed in each orbit when modeling B_r. Revs 251, 252, 255, 257, 258, 261, 263, 265, 267, and 269 are best matched by the first profile. Revs 253 and 254 are best matched by the second profile. Revs 259, 260, 262, 264, and 266 are best matched by the third profile, and Rev 268 is best matched by the fourth profile.

The PPO perturbation fields point radially outward from the planet at $\Psi_{N,S} = 0°$ and radially inward at $\Psi_{N,S} = 180°$ (Andrews et al., 2010; Provan et al., 2012). As aforementioned, large displacements in the position of the current sheet center are observed when the two PPO systems are in phase ($\Delta\Phi = 0°$), that is, pointing in the same direction. Maximum southward displacements are observed in the magnetic field data when the PPO systems point radially outward from the planet and directly toward the spacecraft in the magnetotail, while maximum northward displacements are observed when the PPO systems point radially into the planet and directly away from the spacecraft. Thus, the displaced position of the current sheet center is described by C17 as

$$z^* = -\left[z_N \cos(\Psi_N) + z_S \cos(\Psi_S)\right], \tag{5}$$

where $z_{N,S}$ is the displacement amplitude due to the northern and southern PPO systems individually, which is determined empirically. Equation (5) determines the displacement of the current sheet center with respect to an unperturbed magnetic equator. The unperturbed magnetic equator is taken to lie at $z = z_H$, where z_H is the position of the hinged magnetic equator as described by (Arridge et al., 2008):

$$z_H = \left[\rho - \rho_H \tanh\left(\frac{\rho}{\rho_H}\right)\right] \tan(\lambda_{SUN}). \tag{6}$$

In equation (6), ρ is the perpendicular distance to the spin axis, ρ_H is the "hinging distance" which is approximately the point at which the hinging effect becomes significant in the magnetosphere, and λ_{SUN} is the Sun's latitude at Saturn. The displaced position of the current sheet center relative to z_H is then evaluated by adding equations (5) and (6). Equation (3), scaled by B_{lobe}, then becomes

$$B_r(t) = B_{lobe}(t)\left[a \tanh\left[\frac{z_{sc}(t) - \left[z_H + z^*(t)\right]}{D^*(t)}\right] + \ b \tanh\left[\frac{z_{sc}(t) - \left[z_H + z^*(t)\right]}{cD^*(t)}\right]\right]. \tag{7}$$

Large modulations in the thickness of the current sheet are observed when the two PPO systems are in antiphase ($\Delta\Phi = 180°$), that is, pointing in opposite directions. When the northern system points radially toward the observer, observations have shown a highly thinned current sheet. Alternatively, when the southern system points radially toward the observer, a highly thickened current sheet is observed. These effects are taken to be related to the modulations of the colatitudinal field components in the two systems. The modulated half-thickness of the current sheet is thus described by C17 as

$$D^* = D - \left[D_N \cos(\Psi_N) - D_S \cos(\Psi_S)\right], \tag{8}$$

where D is the unperturbed half-thickness of the current sheet and $D_{N,S}$ is the amplitude of the thickness modulation due to the northern and southern PPO systems, respectively, and determined empirically. It is clear from equation (8) that $D_{N,S}$ must be constrained relative to D such that D^* remains positive throughout the PPO cycle.

The relative strengths of the northern and southern amplitudes in equations (5) and (8) are related by the parameter k, which gives the amplitude ratio of the northern and southern PPO systems (Andrews et al., 2012; Provan et al., 2013, 2016, 2018):

$$k = \frac{z_N}{z_S} = \frac{D_N}{D_S}. \tag{9}$$

For $k >> 1$, the northern PPO system dominates the southern, and vice versa for $k \leq\lessdot 1$. The case where $k = 1$ represents a regime where both systems have an equal effect on the current sheet.

2.2. Parameter Constraints and Initial Analysis

To evaluate the modeled B_r along the spacecraft trajectory from equation (7), we must first constrain the four unknown parameters in the model: k, $z_{N,S}$, $D_{N,S}$, and ρ_H. Hunt et al. (2018) and Provan et al. (2018) determined that $k = 1.29 \pm 0.24$ and k $\sim$ 1.4, respectively, during the F-ring orbits, which is consistent with earlier observations of $k > 1$ during northern summer. Studies that determine k in the equatorial plane from magnetic field measurements have shown that while k is variable with Saturnian season, it is observed to be relatively stable over ~100-day intervals. Hence, we use $k = 1.3$ for this study, assuming that the relative strength of the PPO systems is stable during the F-ring orbits (~6 months) and that the model is predominantly sensitive to changes in PPO beat phase.

The amplitudes of the displacement modulations $z_{N,S}$, thickness modulations $D_{N,S}$, and hinging parameter ρ_H are not known from literature. They are therefore determined by searching a 3-D parameter grid of physically plausible values on a Rev by Rev basis. By performing this analysis on each Rev, any variability in the resulting values of $z_{N,S}$ and $D_{N,S}$ would be indicative of temporal variability in the strength of the PPO systems.

We consider z_N in the range between 0.1 and $0.8R_S$ (in $0.1R_S$ steps), where the corresponding southern amplitudes are given by equation (9). The upper limit on z_N can be understood by studying Figure 1. The B_r reversals on the F-ring orbits are observed over a range of $\Delta z \sim 3R_S$. When the two PPO systems are in phase, the magnetic equator undergoes maximum displacement modulations about a nominal z position; thus, the magnetic equator cannot be displaced by more than $1.5R_S$ in any one direction (half of the observed range), or else B_r reversals would have been observed over a larger Δz range. Rearranging equation (5) for $\cos(\Psi_{N,S}) = \pm 1$ returns an upper limit of $z_N \leq 0.85R_S$ corresponding to $z^* = \pm 1.5R_S$.

We consider D_N in the range between 0.1 and $0.5R_S$ (in $0.1R_S$ steps). As indicated in section 2.1, the upper limit on D_N is determined by enforcing the limit $D^* > 0$ in equation (8). Kellett et al. (2009) determined the half-thickness of the nightside equatorial current sheet to be variable between 0.5 to $2.5R_S$ from three highly inclined Cassini passes. However, PPOs were not well understood at the time of their study, which made it challenging to separate temporal and spatial variability in their discussion. Hence, we assume the unperturbed half-thickness of the magnetotail current sheet to lie within that range and provisionally set it to $D = 1R_S$. Arridge et al. (2011) observed the hinging distance, ρ_H, to be variable between 16 and $32R_S$ over month-long timescales during an interval of southern summer. Assuming that the hinging effect is similarly variable during northern summer (but in the opposite z direction), we consider ρ_H between 16 and $32R_S$ (in $1R_S$ steps) but also explore additional values at $\rho_H = 40$, 60, and $80R_S$.

We evaluate equations (5), (6), and (8) using the aforementioned parameters along the spacecraft trajectory for each Rev in the interval where the spacecraft is outbound between $\rho \simeq 16$ and $21R_S$. The radial field is then modeled using equation (7) for every permutation of z_N, D_N, and ρ_H in our parameter grid, in a northern PPO dominated $k = 1.3$ system, resulting in 800 modeled B_r profiles for every Rev. One of four B_{lobe} profiles is then chosen for scaling the modeled B_r profiles for each Rev as discussed in section 2.1 We then compare the modeled B_r profiles with the magnetic field data in order to constrain $z_{N,S}$, $D_{N,S}$, and ρ_H.

The root mean square error (RMSE) is evaluated between each modeled B_r profile, henceforth B_r* and the smoothed 1-hr running averaged magnetic field data $\langle B_r \rangle$, in order to judge goodness of fit. Contour plots showing the RMSE values of the modeled profiles for each Rev are shown in Figures 3, 4, and 5, where the Revs are organized by beat phase as $\Delta\Phi \sim 0°/360°$ (in phase), $\Delta\Phi \sim 180°$ (antiphase), and $\Delta\Phi \sim 90°/270°$ (quadrature), respectively. The beat phases between the two systems at $16R_S$ and $21R_S$ is shown beside the Rev number for each set of contour plots. The categorization of the Revs in Figures 3–5 specifically employs the first $\Delta\Phi$ shown in the figures, with a $\pm 45°$ margin about the beat phase stated above the color bar in each figure. This is an acceptable approximation, since the PPO beat phases do not change by much (~ 15) in the intervals that we are observing. However, for cases where $\Delta\Phi$ is closer to the limits of the category boundaries, we should expect to see deviations from the "ideal" behavior defined for the category.

Figures 3–5 follow the same format: For every Rev, there are 20 contour plots, each showing the RMSE of the models that were evaluated using the ρ_H value labeled in the panels for Rev 253, 256, and 264 in each figure, respectively. The axes on the contour plots represent the z_N and D_N values within the ranges outlined above, associated with each RMSE data point. The color bar at the top of the figures defines the color scale used in each plot. For a model to be considered a good fit to the data, we choose a limiting RMSE <1.5 nT, similar to the amplitude of the remaining small-timescale structure in $\langle B_r \rangle$ as seen for some Revs in Figure 2. The parameter ranges in which the limiting RMSE holds true are highlighted by the yellow error bars in each contour plot. A yellow circle is then used to indicate the location of the best fit model parameters which correspond to the lowest RMSE in the 3-D parameter space for each Rev, provided this value is <1.5 nT.

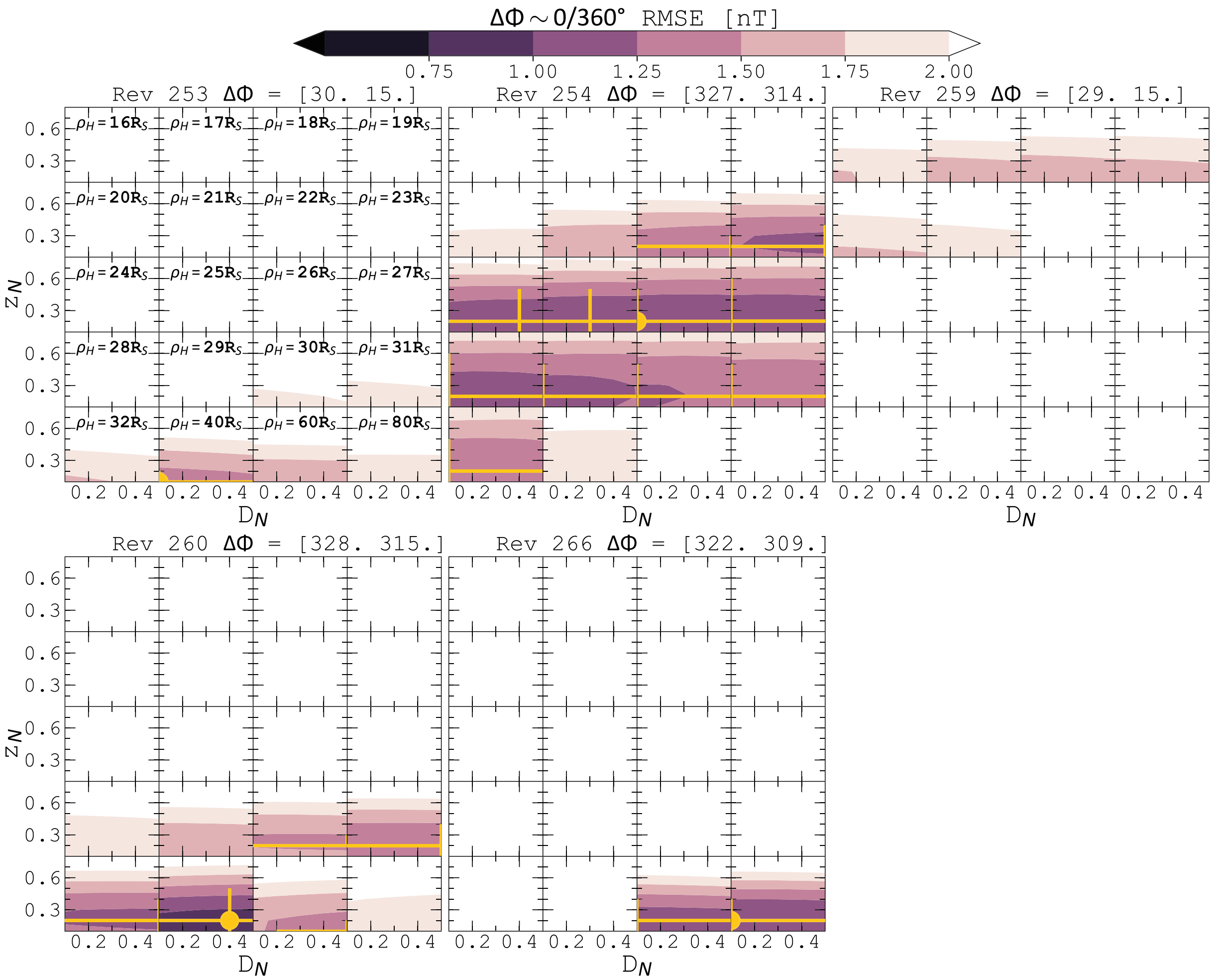

Figure 3. The contour plots show the RMSE values corresponding to each modeled B_r profile for Revs 253, 254, 259, 260, and 266, where the beat phase $\Delta\Phi$ of the PPO systems was approximately 0/360°. The $\Delta\Phi$ at the beginning and end of the interval analyzed (shown in Figure 2) is shown beside the Rev number at the top of the set of 20 contour plots for each Rev. The contours show the RMSE values associated with the modeled B_r* profiles, as a function of the input parameters z_N, D_N, and ρ_H. For a given Rev, each individual contour plot corresponds to models evaluated for a specific ρ_H value (stated on Rev 253), and the axes on the contour plots are the z_N and D_N values employed in the model. The color bar is shown at the top of the figure, and it scales from black (low RMSE) to white (high RMSE) with shades of purple in between. Darker colors indicate a better statistical agreement between the model and the data. A yellow circle is used to identify the location of the model parameters corresponding to the lowest RMSE for each Rev, provided that it is < 1.5 nT. The error bars on the yellow circle indicate the range of z_N and D_N values for which the RMSE between the model and the data is < 1.5 nT. Rev 259 is the only orbit where every modeled profile has an RMSE ≥1.5 nT.

From Figures 3–5 we observe that there are many parameter sets which qualify as good fits, as indicated by the yellow error bars on multiple 2-D contour slices for each Rev. This makes it challenging to constrain the parameters which best describe the physical system, especially in the cases where the model is insensitive to one or more of the parameters, as it is to the thickness modulation parameter D_N under in-phase conditions (Figure 3) and to the displacement modulation parameter z_N under antiphase conditions (Figure 4).

For example, all the Revs in Figure 3 are better fit by models where z_N is in the range 0.1–0.6R_S, but the model is insensitive to the value of D_N for 4 out of 5 Revs as the two PPO systems are approximately in phase. The cosines in equation (8) would subtract from one another when $\Psi_N \sim \Psi_S$ and the model becomes insensitive to the thickness modulation amplitudes. Similarly for the Revs presented in Figure 4, where the PPO systems were close to being in antiphase, for all but one case, the model appears to be insensitive to the value of z_N as the cosines in equation (5) subtract from one another when $\Delta\Phi = 180°$, thus making the model insensitive to the displacement modulation amplitudes. The RMSE contours of the modeled profiles for the Revs shown in Figure 5 for near-quadrature conditions show a much stronger preference for certain z_N and

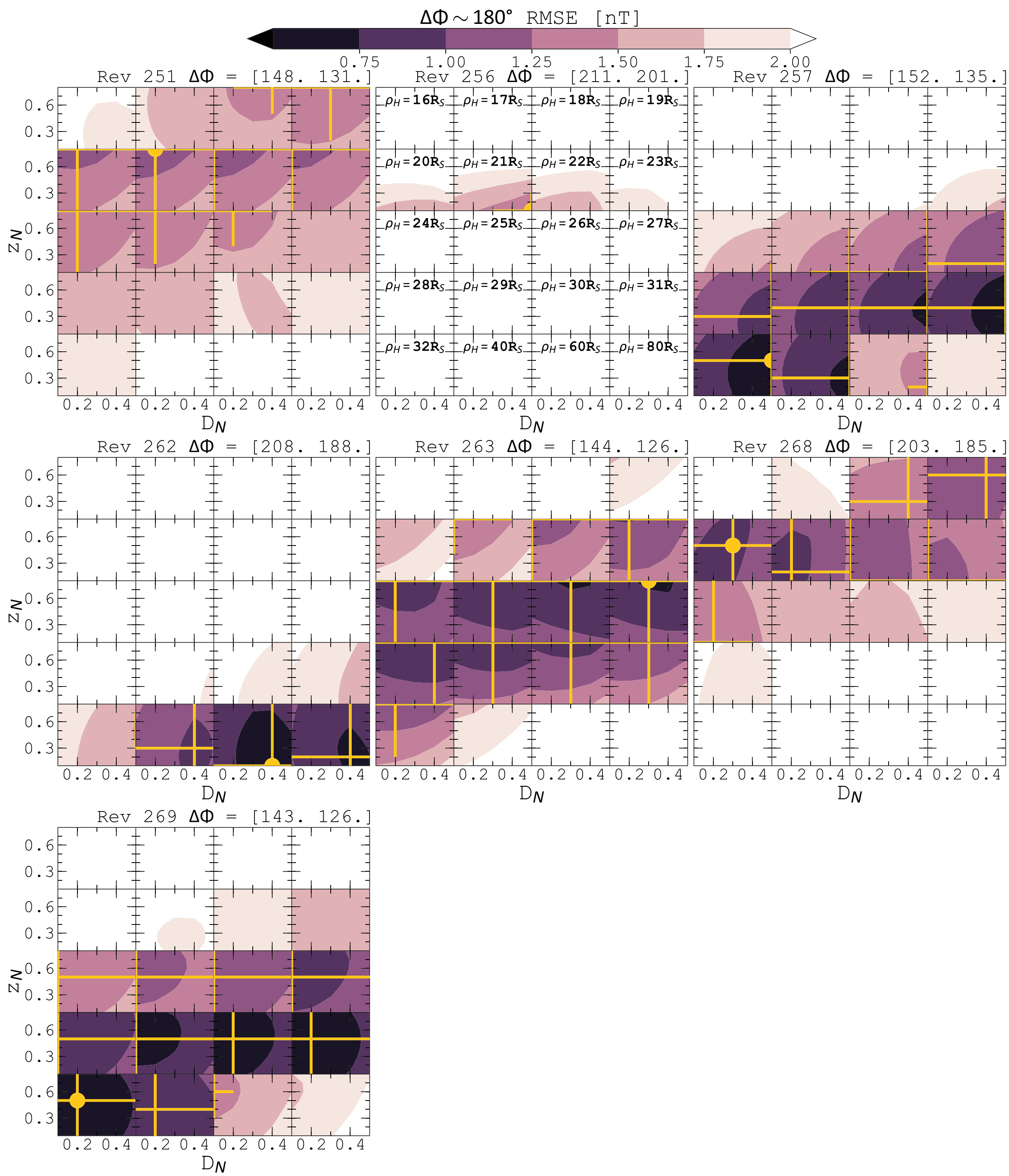

Figure 4. The contour plots show the RMSE values corresponding to each modeled B_r profile for Revs 251, 256, 257, 262, 263, 268, and 269, where the beat phase of the PPO systems was approximately 180°. The format of the figure is the same as Figure 3.

D_N parameter combinations, although the yellow error bars still imply that a good fit could be achieved by using a wide range of parameter combinations in our physically constrained range of z_N and D_N values.

We now consider the implications of the overall result shown in Figures 3–5 and begin by noting that there are modeled profiles which fit the data well for most of the F-ring orbits for z_N in the range 0.3–0.5R_S and D_N in the range 0.3–0.5R_S as well. Rev 253 is an exception, where only $z_N = 0.1R_S$ yields B_r* profiles with RMSE <1.5 nT. However, there are many small-timescale fluctuations ≥2 nT present in both B_r and $\langle B_r \rangle$ for Rev

10.1029/2019JA027371

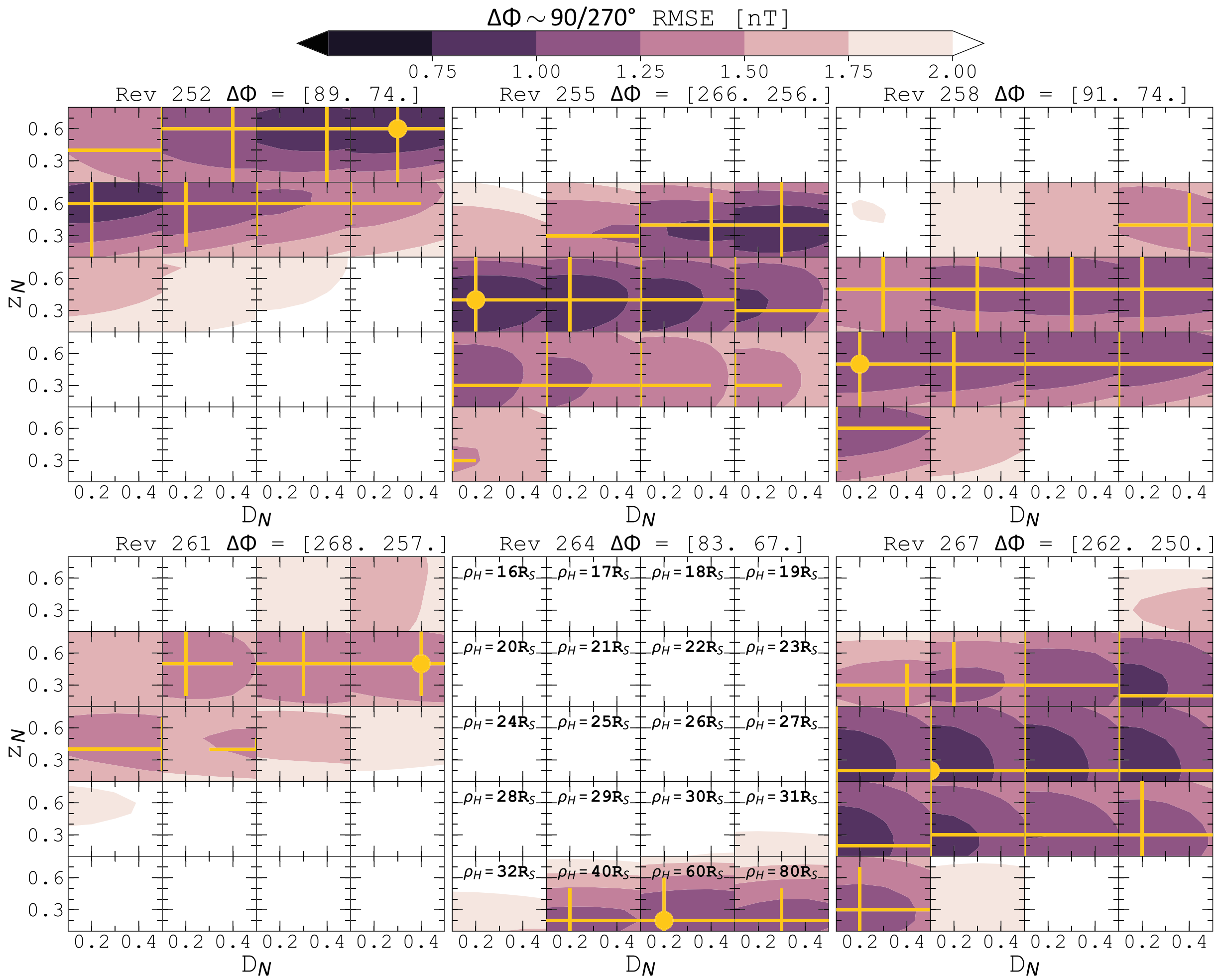

Figure 5. The contour plots show the RMSE values corresponding to each modeled B_r profile for Revs 252, 255, 258, 261, 264, and 267, where the beat phase of the PPO systems was approximately 90/270°. The format of the figure is the same as Figure 3.

253 as shown in Figure 2, indicating the presence of non-PPO dynamical processes and, therefore, making it a less reliable indicator of PPO-driven dynamics. Rev 259 is the other exception, where the modeled profiles all yield an RMSE ≥1.5 nT. Analysis of all the contour plots clearly shows that the F-ring orbits cannot all be well described by a unique set of model parameters. For example, if we were to set $z_N, D_N = (0.4, 0.4)R_S$ as an average state of the system, the model would no longer match the data well for Rev 256, where good agreement is only found in the very specific case of $z_N, D_N = (0.3, 0.5)R_S$ in the constrained parameter range.

The variability in the range of well-fitting PPO model parameters for every Rev indicates that the temporal variability observed in the magnetic field data cannot be understood by solar wind hinging and variable PPO beat phases alone. Instead, it is likely that the strength of the PPO systems are also temporally variable which introduces additional variability into the system. Thus, it would be physical to allow z_N and D_N to vary in a range of values which are repeatable across the different Revs in order to capture the temporal variability in the strength of the PPO systems. Hence, we further constrain z_N and D_N to lie the range 0.3–0.5R_S. For any given Rev, there are generally multiple values of ρ_H for which the modeled radial profiles have an RMSE <1.5 nT, and the range of ρ_H values which qualify as good statistical fits to the data is also variable from orbit to orbit. Therefore, we are unable to further constrain the range of ρ_H values considered in this study, and we seek the parameter combination which minimizes the RMSE between B_r* and $\langle B_r \rangle$ within the restricted range of $z_N, D_N = 0.3 - 0.5R_S$ for ρ_H in the range 16 to 80R_S (with steps as described previously).

3. Results and Discussion

The best fit modeling results for Revs 251–269 (excluding Rev 265) from equation (7), B_r*, based on the considerations in section 2.2, are shown by dashed orange lines in the top panels corresponding to each Rev in Figure 6. The model parameters employed are given in each panel. In the same panel, the 1-min and 1-hr averaged radial magnetic field, B_r and $\langle B_r \rangle$, are shown as solid gray and solid blue lines, respectively. The RMSE values quoted in each panel correspond to the agreement between the B_r* and $\langle B_r \rangle$ shown, as previously discussed. The lower panels for each Rev illustrate the modulated modeled current sheet versus time, together with the spacecraft trajectory through it (solid orange line). The position of the displaced magnetic equator z_H for the best fit hinging distance ρ_H is evaluated using equation (6) and shown by a dot-dashed green line. The dashed black line then shows the position of the displaced current sheet center ($z_H + z^*$), while the solid thick gray lines show the upper and lower edge of the PPO modulated current sheet ($z^* \pm D^*$).

The constants a and b defined in equation (3) were modified to 0.8 and 0.2, respectively, in the modeled profiles shown, which is in approximate agreement with the values suggested by (Cowley and Provan, 2017), but the modified values provide a slightly sharper boundary between the main current layer and the diffuse current layer, which provides better visual agreement with the observations.

Overall, it can be seen that the model provides a very good fit to the variable current sheet fields shown in Figure 6, both with regard to the timing of the crossings and the highly variable form of the observed radial magnetic fields. For all 18 F-ring orbits considered in this study, the orbit-to-orbit variability in large-scale structure of the observed B_r profiles can be explained by a magnetotail current sheet experiencing periodic modulations due to the variable configuration and strength of the dual PPO systems, together with variable solar wind forcing (variable ρ_H).

The B_r reversals and the PPO oscillations are in very good agreement between the modeled profiles and the data, with the exception of Revs 253, 256, and 259, where the RMSE associated with the best fit B_r* profiles is ≥1.5 nT, implying a poor statistical fit. However, visual inspection shows that the large-scale structure of Revs 253, 256, and 259 is generally well reproduced by the model but that there are other perturbation sources present, such as passing plasmoids (Jackman et al., 2014) or magnetotail reconnection events (Thomsen et al., 2015), which introduce additional structure to the observed magnetic field which is not entirely smoothed out in $\langle B_r \rangle$. These Revs will be discussed in more detail later in this section.

There is some orbit-to-orbit variability in the RMSE of the best fit models presented in Figure 6, which is associated with the small-timescale fluctuations in the radial magnetic field. For example, the RMSE of the best fit model for Rev 251 is 1.3 nT, where small-timescale fluctuations of 1–2 nT of amplitude are present in $\langle B_r \rangle$, as compared to Rev 269, where $\langle B_r \rangle$ is overall much smoother and the best fit model RMSE is 0.5 nT. However, the overall excellent visual agreement between the modeled profiles and the data in Figure 6 show that the limiting RMSE of 1.5 nT chosen earlier in our analysis is a valid indicator of goodness of fit. The overall agreement in the amplitudes of B_r* and $\langle B_r \rangle$ also validates the provisional half-thickness $D = 1R_S$ employed in this study.

Analysis of the best fit z_N, D_N, and ρ_H parameters in the top panels of Figure 6 shows that the PPO modulations of the magnetotail current sheet are very well constrained by displacement and thickness modulation amplitudes of 0.3–0.5R_S for the northern PPO system in a $k = 1.3$ regime, with some temporal variability from orbit to orbit. The ρ_H values, however, are highly variable from orbit to orbit, as seen in best fit ρ_H values for Revs 260–262, which vary from 40R_S, to 23R_S, to 60R_S in consecutive orbits which are approximately a week apart. The temporal variability in ρ_H is consistent with the findings of Arridge et al. (2011) and can be understood by considering north-south deflections in the solar wind flow, as well as variable solar wind pressure.

The range of ρ_H values considered in this study is, however, larger than the range of values determined by Arridge et al. (2011) during southern summer at Saturn ($\rho_H = 16 - 32R_S$). Figure 6 shows that for ∼30% of the F-ring orbits (Revs 253, 260, 262, 264, and 266), the magnetic field data are best fit by models with $\rho_H > 32R_S$. The bottom panels for these Revs show that the position of the unperturbed magnetic equator, z_H, is very close to $z = 0R_S$, which implies very little to no solar wind forcing in these cases, which is unexpected for northern summer conditions (Arridge et al., 2008), but again, could also be explained by short-term deflections in the direction of solar wind flow.

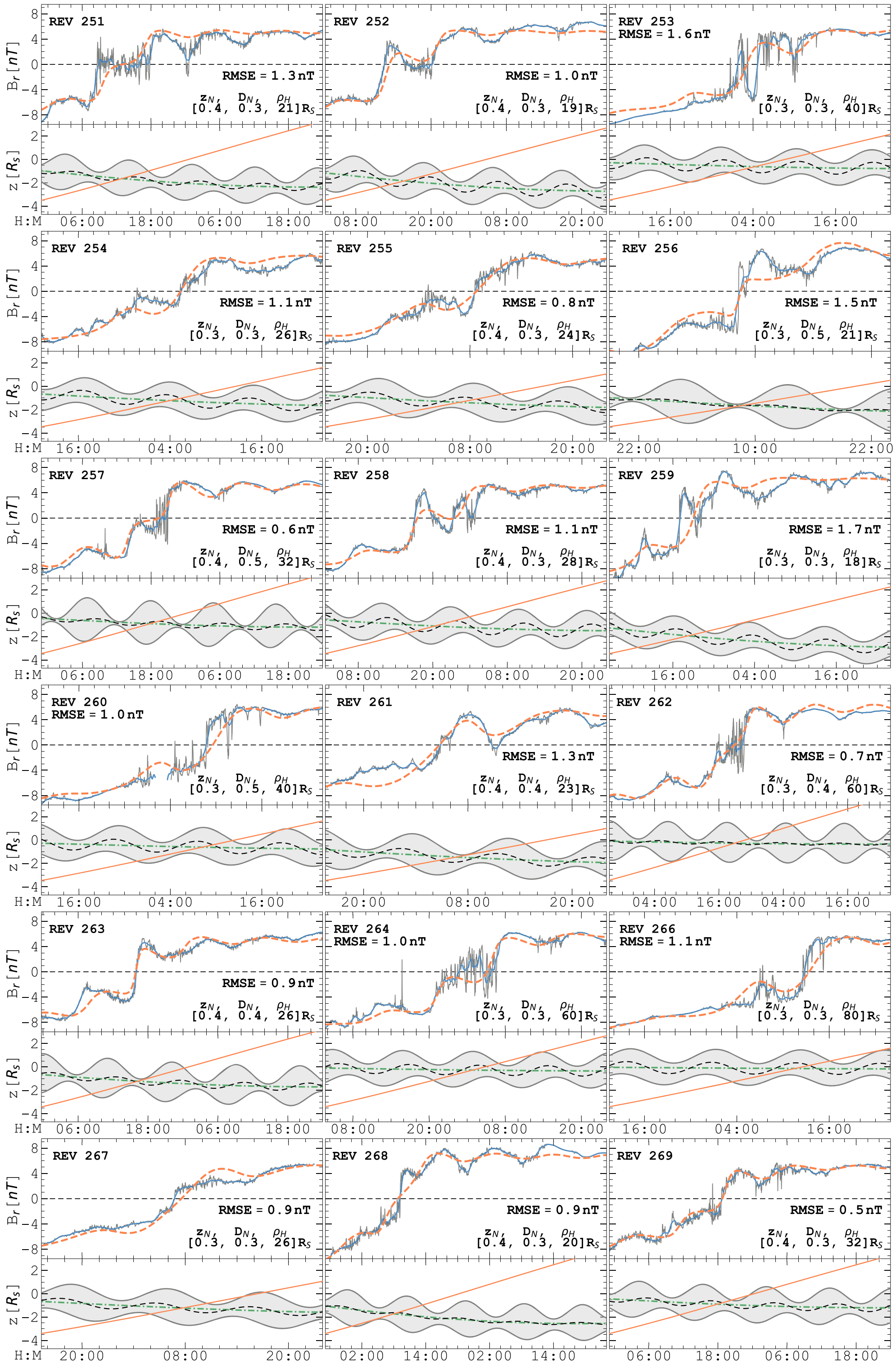

Figure 6. Two panels are shown for each Rev. The top panels show B_r, $\langle B_r \rangle$ (as in Figure 2), with the best fit modeled radial field, B_r*, superposed as a dashed orange line. The model parameters and RMSE value corresponding to best fit B_r* are included in these panels. The bottom panels for each Rev illustrate the PPO modulated current sheet (shaded region) associated with the best fit B_r* along the spacecraft trajectory (solid orange line). The position of the hinged magnetic equator z_H (dot-dashed green line) corresponds to the ρ_H value in the top panels. The position of the displaced current sheet center ($z_H \pm z^*$) is shown by a dashed black line. The thick gray lines show the upper and lower boundaries of the PPO modulated current sheet ($z_H + z^* \pm D^*$).

10.1029/2019JA027371

As previously mentioned, Figures 3–5 show that there is usually a range of ρ_H values which fits the data well for every Rev, and this range is highly variable from orbit to orbit, with no obvious organization by beat phase. However, we note that the range of ρ_H values that fit the data well can generally be grouped into one of three categories: $\rho_H = 16 - 23R_S$, where z_H lies between -2 and $-1R_S$ at $\sim 18R_S$; $\rho_H = 23 - 32R_S$, where z_H lies between -1 and $-0.5R_S$; and $32 - 80R_S$, where z_H lies between -0.5 and $0R_S$.

For the in-phase cases (Figure 3) we find that Rev 259 is well fit by smaller ρ_H values, Rev 254 is well fit by the middle range of ρ_H values, whereas Revs 253, 260, and 266 are well fit by the larger ρ_H values. For the antiphase cases (Figure 4), Revs 251, 256, and 268 are well fit by the smaller ρ_H values; Revs 257, 263, and 269 are better fit by the middle range of ρ_H values; and only Rev 262 is well fit by larger ρ_H values. For the near-quadrature cases (Figure 5), Revs 252 and 261 are well fit by smaller ρ_H values; Revs 255, 258, and 267 are well fit by the middle range ρ_H values; and only Rev 264 is well fit by larger ρ_H values.

Based on these groupings, it appears as though smaller and middle range ρ_H values are more common when the beat phase of the PPO systems is near antiphase or quadrature, when the thickness of the current sheet is temporally variable over PPO dynamic timescales (~2 hr). Conversely, larger values of ρ_H generally fit the data better for the in-phase Revs, when the thickness of the current sheet is temporally static over short-term intervals. However, due to the small sample size considered in each beat phase category, it is difficult to draw any definite conclusions from this analysis.

The amplitude of the PPO modulation in the B_r* profiles for spacecraft positions north of the current sheet center is very weak for Revs 251, 252, 259, and 268, where the data are best fit by $\rho_H < 20R_S$. However, the disparity between amplitude of the PPO oscillations in the model and the data is to be expected. As mentioned in section 1, Provan et al. (2012) show that while the magnetic field in the equatorial region is dually modulated by the two PPO systems, the northern and southern lobes are individually modulated by the northern and southern PPO systems, respectively. Hence, the results from the C17 model are most accurate in the equatorial region, where the dual-modulation approximation holds true. It can be seen, for example, from the bottom panel for Rev 259 in Figure 6 that the spacecraft is ~3–4R_S away from the magnetic equator toward the end of the interval shown.

As indicated in section 1.1, small-timescale fluctuations on the order of 10–20 min are present in the magnetic field data, where for certain Revs, these fluctuations correspond to quick reversals in B_r. These fluctuations occur on much shorter timescales than the expected PPO dynamic timescale; thus, it was assumed in section 1.1 that they were caused by other magnetic perturbation sources affecting the magnetotail. However, examination of Revs 251, 257, 262, and 264 in Figure 6, where the small-timescale fluctuations are most prominent, shows that these fluctuations correspond to intervals where the spacecraft is at the center of a thick current sheet for an extended interval of time (as illustrated in the bottom panels for each Rev). There is also an increase in smaller amplitude small-timescale structure when the spacecraft is close to the center of the current sheet for a shorter interval, for example, Revs 252, 255, and 269. This behavior thus indicates the presence of rapid oscillatory behavior of the magnetic field near the weak-field center of the current sheet. Nevertheless, such behavior does not always appear to be present, as in the case of Revs 254 and 267. Further study of this phenomenon is therefore required but is beyond the scope of this study.

The modeled outputs for Revs 253, 256, and 259 in Figure 6 return an RMSE ≥1.5 nT. The first reversal observed in B_r for Rev 259 is not well fit by the model, and the model lags behind the data by ~1–2 hr as seen near the 20-hr mark in the data (second B_r reversal) and the 4-hr mark while $B_r > 0$ nT. Even so, comparison of $\langle B_r \rangle$ to B_r* shows that the large-scale structure of the magnetic field data is generally well captured by the model and that the first reversal in B_r appears to be an additional short-term perturbation to the displacement of the magnetic equator due to non-PPO-related perturbation sources. This effect is also observed in Revs 253, 256, and 258, where the best fit B_r* profiles in Figure 6 generally match the magnitude and profile of $\langle B_r \rangle$ well; however, fluctuations on the order of ~30–100 min in B_r (larger than the cases where the best fit B_r* yielded an RMSE <1.5 nT) indicate that the magnetotail current sheet is dually modulated by the PPO systems as well as additional perturbation sources that displace the magnetic equator in the north-south direction on timescales shorter than the expected PPO dynamic timescales (>2 hr). Such perturbations could be attributed to ripples on the surface on the current sheet (Martin and Arridge, 2017) (an effect that cannot be reproduced by a simple Harris current sheet model) or passing plasmoids in the magnetotail current sheet (Jackman et al., 2014).

4. Conclusions

The aim of this study was to investigate the orbit-to-orbit variability observed near apoapsis in the radial magnetic field component B_r during the F-ring orbits. We find that for all 18 F-ring orbits considered in this study, the large-scale variability in the B_r profile is well modeled by considering a magnetotail current sheet which undergoes periodic thickness and displacement modulations due to two magnetic perturbation systems known as PPOs, where the northern perturbations dominate the southern by a ratio of $k = 1.3$ (Hunt et al., 2018; Provan et al., 2018), combined with a temporally variable southward displacement of the magnetotail current sheet (Arridge et al., 2008, 2011) due to solar wind forcing. The amplitudes of the thickness modulation D_N and displacement modulation z_N due to the northern PPO system were both found to be very well constrained in the range 0.3–0.5R_S, respectively, with slight temporal variability within those ranges on a Rev by Rev basis. The position of the unperturbed displaced magnetic equator z_H is found to be variable between ~ -2 and $0R_S$, which corresponds to hinging distances of $\rho_H = 16 - 80R_S$.

The excellent overall fits to the large-scale behavior of the radial magnetic field also highlight features in the data that are not contained within the model. One such effect is the small-timescale fluctuations on the order of ∼10–20 min that are observed in the magnetic field data which were variable in amplitude but occurred on timescales significantly shorter than PPO modulation timescales. In our discussion, these fluctuations are found to correspond to intervals where the spacecraft is at the center of a thick current sheet for an extended interval of time, which is associated with multiple, consecutive reversals in B_r, that were observed in 7 of the 18 F-ring orbits.

Revs 253, 256, 258, and 259 are examples of Revs where additional fluctuations and features are present in the magnetic field data on the order of ∼30–100 min which could not be captured by our model, thus indicating the presence of additional perturbation sources which affect the dynamics of the magnetotail current sheet. Variable compressional states of the magnetosphere, passing plasmoids/dipolarizations, ripples on the surface of the current sheet, or closure of the auroral field-aligned currents are a few other processes in the magnetosphere which could perturb the magnetotail current sheet on variable timescales; however, investigating these perturbation sources is beyond the scope of our study.

Acknowledgments

O. A. is supported by a STFC studentship. G. J. H. is supported by STFC Grant ST/N000692/1. Work at the University of Leicester was supported by STFC Grant ST/N000749/1. M. K. D. is funded by Royal Society Research ProfessorshipRP140004. Calibrated magnetic field data from the Cassini mission are available from the NASA Planetary Data System at the Jet Propulsion Laboratory (https://pds.jpl.nasa.gov/).

References

Andrews, D. J., Bunce, E. J., Cowley, S. W. H., Dougherty, M. K., Provan, G., & Southwood, D. J. (2008). Planetary period oscillations in Saturn's magnetosphere: Phase relation of equatorial magnetic field oscillations and Saturn kilometric radiation modulation. *Journal of Geophysical Research*, *113*, A09205. https://doi.org/10.1029/2007JA012937

Andrews, D. J., Coates, A. J., Cowley, S. W. H., Dougherty, M. K., Lamy, L., Provan, G., & Zarka, P. (2010). Magnetospheric period oscillations at Saturn: Comparison of equatorial and high-latitude magnetic field periods with north and south Saturn kilometric radiation periods. *Journal of Geophysical Research*, *115*, A12252. https://doi.org/10.1029/2010JA015666

Andrews, D. J., Cowley, S. W. H., Dougherty, M. K., Lamy, L., Provan, G., & Southwood, D. J. (2012). Planetary period oscillations in Saturn's magnetosphere: Evolution of magnetic oscillation properties from southern summer to post-equinox. *Journal of Geophysical Research*, *117*, A04224. https://doi.org/10.1029/2011JA017444

Arridge, C. S., André, N., Khurana, K. K., Russell, C. T., Cowley, S. W. H., Provan, G., et al. (2011). Periodic motion of Saturn's nightside plasma sheet. *Journal of Geophysical Research*, *116*, A11205. https://doi.org/10.1029/2011JA016827

Arridge, C. S., Khurana, K. K., Russell, C. T., Southwood, D. J., Achilleos, N., Dougherty, M. K., et al. (2008). Warping of Saturn's magnetospheric and magnetotail current sheets. *Journal of Geophysical Research*, *113*, A08217. https://doi.org/10.1029/2007JA012963

Carbary, J. F., & Mitchell, D. G. (2013). Periodicities in Saturn's magnetosphere. *Reviews of Geophysics*, *51*, 1–30. https://doi.org/10.1002/rog.20006

Connerney, J. E. P., Acuña, M. H., & Ness, N. F. (1981). Modeling the Jovian current sheet and inner magnetosphere. *Journal of Geophysical Research*, *86*(A10), 8370–8384. https://doi.org/10.1029/ja086ia10p08370

Cowley, S. W. H., & Provan, G. (2015). Planetary period oscillations in Saturn's magnetosphere: Comments on the relation between post-equinox periods determined from magnetic field and SKR emission data. *Annales Geophysicae*, *33*(7), 901–912. https://doi.org/10.5194/angeo-33-901-2015

Cowley, S. W. H., & Provan, G. (2016). Planetary period oscillations in Saturn's magnetosphere: Further comments on the relationship between post-equinox properties deduced from magnetic field and Saturn kilometric radiation measurements. *Icarus*, *272*(7), 258–276. https://doi.org/10.1016/j.icarus.2016.02.051

Cowley, S. W. H., & Provan, G. (2017). Planetary period modulations of Saturn's magnetotail current sheet during northern spring: Observations and modeling. *Journal of Geophysical Research: Space Physics*, *122*, 6049–6077. https://doi.org/10.1002/2017JA023993

Cowley, S. W. H., Provan, G., Hunt, G. J., & Jackman, C. M. (2017). Planetary period modulations of Saturn's magnetotail current sheet: A simple illustrative mathematical model. *Journal of Geophysical Research: Space Physics*, *122*, 258–279. https://doi.org/10.1002/2016JA023367

Dougherty, M. K., Cao, H., Khurana, K. K., Hunt, G. J., Provan, G., Kellock, S., et al. (2018). Saturn's magnetic field revealed by the Cassini Grand Finale. *Science*, *362*(6410), eaat5434. https://doi.org/10.1126/science.aat5434

Gurnett, D. A. (2011). An SLS4 longitude system based on a tracking filter analysis of the rotational modulation of Saturn Kilometric Radiation. *PLANETARY RADIO EMISSIONS VII*, 51–64. https://doi.org/10.1553/PRE7s51

Gurnett, D. A., Lecacheux, A., Kurth, W. S., Persoon, A. M., Groene, J. B., Lamy, L., et al. (2009). Discovery of a north-south asymmetry in Saturn's radio rotation period. *Geophysical Research Letters*, *36*, L16102. https://doi.org/10.1029/2009GL039621

Hunt, G. J., Cowley, S. W., Provan, G., Bunce, E. J., Alexeev, I. I., Belenkaya, E. S., et al. (2014). Field-aligned currents in Saturn's southern nightside magnetosphere: Subcorotation and planetary period oscillation components. *Journal of Geophysical Research: Space Physics*, *119*, 9847–9899. https://doi.org/10.1002/2014JA020506

Hunt, G. J., Cowley, S. W., Provan, G., Bunce, E. J., Alexeev, I. I., Belenkaya, E. S., et al. (2016). Field-aligned currents in Saturn's magnetosphere: Local time dependence of southern summer currents in the dawn sector between midnight and noon. *Journal of Geophysical Research: Space Physics*, *121*, 7785–7804. https://doi.org/10.1002/2016JA022712

Hunt, G. J., Cowley, S. W. H., Provan, G., Bunce, E. J., Alexeev, I. I., Belenkaya, E. S., et al. (2015). Field-aligned currents in Saturn's northern nightside magnetosphere: Evidence for interhemispheric current flow associated with planetary period oscillations. *Journal of Geophysical Research: Space Physics*, *120*, 7552–7584. https://doi.org/10.1002/2015JA021454

Hunt, G. J., Provan, G., Bunce, E. J., Cowley, S. W. H., Dougherty, M. K., & Southwood, D. J. (2018). Field-aligned currents in Saturn's magnetosphere: Observations from the F-ring orbits. *Journal of Geophysical Research: Space Physics*, *123*, 3806–3821. https://doi.org/10.1029/2017JA025067

Jackman, C. M., & Arridge, C. S. (2011). Statistical properties of the magnetic field in the Kronian magnetotail lobes and current sheet. *Journal of Geophysical Research*, *116*, A05224. https://doi.org/10.1029/2010JA015973

Jackman, C. M., Arridge, C. S., McAndrews, H. J., Henderson, M. G., & Wilson, R. J. (2009). Northward field excursions in Saturn's magnetotail and their relationship to magnetospheric periodicities. *Geophysical Research Letters*, *36*, L16101. https://doi.org/10.1029/2009GL039149

Jackman, C. M., Slavin, J. A., Kivelson, M. G., Southwood, D. J., Achilleos, N., Thomsen, M. F., et al. (2014). Saturn's dynamic magnetotail: A comprehensive magnetic field and plasma survey of plasmoids and traveling compression regions and their role in global magnetospheric dynamics. *Journal of Geophysical Research: Space Physics*, *119*, 5465–5494. https://doi.org/10.1002/2013JA019388

Jia, X., & Kivelson, M. G. (2012). Driving Saturn's magnetospheric periodicities from the upper atmosphere/ionosphere: Magnetotail response to dual sources. *Journal of Geophysical Research*, *117*, A11219. https://doi.org/10.1029/2012JA018183

Kellett, S., Bunce, E. J., Coates, A. J., & Cowley, S. W. (2009). Thickness of Saturn's ring current determined from north-south Cassini passes through the current layer. *Journal of Geophysical Research*, *114*, A04209. https://doi.org/10.1029/2008JA013942

Khurana, K. K., Mitchell, D. G., Arridge, C. S., Dougherty, M. K., Russell, C. T., Paranicas, C., et al. (2009). Sources of rotational signals in Saturn's magnetosphere. *Journal of Geophysical Research*, *114*, A02211. https://doi.org/10.1029/2008JA013312

Kurth, W. S., Averkamp, T. F., Gurnett, D. A., Groene, J. B., & Lecacheux, A. (2008). An update to a Saturnian longitude system based on kilometric radio emissions. *Journal of Geophysical Research*, *113*, A05222. https://doi.org/10.1029/2007JA012861

Kurth, W. S., Lecacheux, A., Averkamp, T. F., Groene, J. B., & Gurnett, D. A. (2007). A Saturnian longitude system based on a variable kilometric radiation period. *Geophysical Research Letters*, *34*, L02201. https://doi.org/10.1029/2006GL028336

Lamy, L. (2011). Variability of southern and northern periodicities of Saturn Kilometric Radiation, Planetary Radio Emissions VII.

Lamy, L. (2017). The Saturnian Kilometric Radiation before the Cassini Grand Finale. https://doi.org/10.1553/PRE8s171

Martin, C. J., & Arridge, C. S. (2017). Cassini observations of aperiodic waves on Saturn's magnetodisc. *Journal of Geophysical Research: Space Physics*, *122*, 8063–8077. https://doi.org/10.1002/2017JA024293

Morooka, M. W., Modolo, R., Wahlund, J. E., André, M., Eriksson, A. I., Persoon, A. M., et al. (2009). The electron density of Saturn's magnetosphere. *Annales Geophysicae*, *27*, 2971–2991. https://doi.org/10.5194/angeo-27-2971-2009

Provan, G., Andrews, D. J., Arridge, C. S., Coates, A. J., Cowley, S. W. H., Cox, G., et al. (2012). Dual periodicities in planetary-period magnetic field oscillations in Saturn's tail. *Journal of Geophysical Research*, *117*, 1–20. https://doi.org/10.1029/2011JA017104

Provan, G., Cowley, S. W., Lamy, L., Bunce, E. J., Hunt, G. J., Zarka, P., & Dougherty, M. K. (2016). Planetary period oscillations in Saturn's magnetosphere: Coalescence and reversal of northern and southern periods in late northern spring. *Journal of Geophysical Research: Space Physics*, *121*, 9829–9862. https://doi.org/10.1002/2016JA023056

Provan, G., Cowley, S. W. H., Bradley, T. J., Bunce, E. J., Hunt, G. J., & Dougherty, M. K. (2018). Planetary period oscillations in Saturn's magnetosphere: Cassini magnetic field observations over the northern summer solstice interval. *Journal of Geophysical Research: Space Physics*, *123*, 3859–3899. https://doi.org/10.1029/2018ja025237

Provan, G., Cowley, S. W. H., Sandhu, J., Andrews, D. J., & Dougherty, M. K. (2013). Planetary period magnetic field oscillations in Saturn's magnetosphere: Postequinox abrupt nonmonotonic transitions to northern system dominance. *Journal of Geophysical Research: Space Physics*, *118*, 3243–3264. https://doi.org/10.1002/jgra.50186

Provan, G., Lamy, L., Cowley, S. W., & Dougherty, M. K. (2014). Planetary period oscillations in Saturn's magnetosphere: Comparison of magnetic oscillations and SKR modulations in the postequinox interval. *Journal of Geophysical Research: Space Physics*, *119*, 7380–7401. https://doi.org/10.1002/2014JA020011

Provan, G., Lamy, L., Cowley, S. W. H., & Bunce, E. J. (2019). Planetary period oscillations in Saturn's magnetosphere: Comparison of magnetic and SKR modulation periods and phases during northern summer to the end of the Cassini mission. *Journal of Geophysical Research: Space Physics*, *124*, 1157–1172. https://doi.org/10.1029/2018JA026079

Southwood, D. J., & Cowley, S. W. (2014). The origin of Saturn's magnetic periodicities: Northern and southern current systems. *Journal of Geophysical Research: Space Physics*, *119*, 1563–1571. https://doi.org/10.1002/2013JA019632

Southwood, D. J., & Kivelson, M. G. (2007). Saturnian magnetospheric dynamics: Elucidation of a camshaft model. *Journal of Geophysical Research*, *112*, A12222. https://doi.org/10.1029/2007JAO12254

Szego, K., Nemeth, Z., Foldy, L., Cowley, S. W. H., & Provan, G. (2013). Dual periodicities in the flapping of Saturn's magnetodisk. *Journal of Geophysical Research: Space Physics*, *118*, 2883–2887. https://doi.org/10.1002/jgra.50316

Thomsen, M. F., Jackman, C. M., Cowley, S. W., Jia, X., Kivelson, M. G., & Provan, G. (2017). Evidence for periodic variations in the thickness of Saturn's nightside plasma sheet. *Journal of Geophysical Research: Space Physics*, *122*, 280–292. https://doi.org/10.1002/2016JA023368

Thomsen, M. F., Jackman, C. M., Mitchell, D. G., Hospodarsky, G., Kurth, W. S., & Hansen, K. C. (2015). Sustained lobe reconnection in Saturn's magnetotail. *Journal of Geophysical Research: Space Physics*, *120*, 10,257–10,274. https://doi.org/10.1002/2015JA021768